Double-differential primary target neutron yields from dual-thick-target proton and heavy ion accelerator experiments

Hunter N. Ratliff[a,b,*], Natalie A. McGirl[a], Matthew R. Beach[c], Luis A. Castellanos[a], Martha S. Clowdsley[d], Lawrence H. Heilbronn[a], Chiara LaTessa[e,f], John W. Norbury[d], Adam Rusek[g], Michael Sivertz[g], Ashwin P. Srikrishna[a], Hui-Chen Wang[a], Cary Zeitlin[h]

[a]*Nuclear Engineering Department, University of Tennessee, 1412 Circle Dr., Knoxville, TN 37916, USA*
[b]*Japan Atomic Energy Agency, 2-4 Shirakata, Tokai, Naka, Ibaraki 319-1195, Japan*
[c]*National Institute of Aerospace, 100 Exploration Way, Hampton, VA 23666, USA*
[d]*National Aeronautics and Space Administration Langley Research Center, Hampton, VA 23681-2199, USA*
[e]*University of Trento, Via Calepina, 14-38122 Trento TN, Italy*
[f]*TIFPA - INFN, Via Sommarive, 14-38123 Povo, Trento TN, Italy*
[g]*Brookhaven National Laboratory, PO Box 5000, Upton, NY, 11973-5000, USA*
[h]*Leidos, Inc., 2625 Bay Area Blvd., Houston, TX 77058, USA*

Abstract

Recent experiments at the NASA Space Radiation Laboratory were performed to develop a benchmark dataset relevant to space radiation shielding scenarios by bombarding aluminum and polyethylene targets with galactic cosmic ray-like ion beams. Unique to this experiment, a dual-target configuration was used to emulate an enclosed environment in space in which the radiation environment must be characterized. Neutrons produced by interactions in both thick targets were detected and characterized; this paper discusses the neutrons produced in the most upstream of the two thick targets, detailing the role of source ion and target configuration on neutron yield.

Keywords: neutron, space radiation, shielding, benchmark, time-of-flight

1. Introduction

Prior simulations using a variety of modern particle transport codes predicted the existence of an optimal shielding thickness for aluminum spacecraft walls, around 20-30 g/cm^2, which minimized dose equivalent in the galactic cosmic ray (GCR) induced radiation environment within an enclosed environment in deep space [1]. Beyond this optimal thickness, the dose equivalent was found to increase as the thickness increased, primarily due to a buildup of neutrons and other light ions produced in the "back wall" of the environment. When simulating polyethylene shielding instead, no optimal thickness emerged; though, the rate at which the dose equivalent decreased with increasing polyethylene shield thickness leveled off after thicknesses between 20 and 30 g/cm^2. This can be considered the optimal thickness in the sense that additional shielding would yield marginal benefits in comparison to the increased costs associated with additional mass. The weighting factors for the dose equivalent calculations are based on ICRP 60 [2] and are point values (i.e., not inside a human phantom).

Although the models used in Reference 1 all predict the general feature of a minimum dose equivalent at 20-30 g/cm^2 of aluminum, there are differences in the calculated doses between the models, especially as the shielding thickness increases beyond 20-30 g/cm^2. Because of the complex nature of the GCR environment, a direct comparison between model predictions and measurement is not possible. However, measurements can be conducted at accelerator facilities in which beams of selected ions and energies representing significant components of the GCR flux are bombarded upon thick shields, creating a secondary radiation field that can be characterized experimentally. The measured data is then used for uncertainty quantification and model verification through direct comparison to model predictions of the experiment.

Measurements were conducted at the NASA Space Radiation Laboratory (NSRL), located on the campus of Brookhaven National Laboratory. Double differential thick-target yields of neutrons and light ions (Z≤2) were determined from fifteen GCR-like source beams incident upon eight different shielding configurations. Unique to this experiment was the dual-target system employed wherein a secondary target was placed several meters downstream of the primary target, allowing penetrating source ions and the fragments from interactions in the primary target to then travel downstream and interact in this secondary target. This dual-target configuration was designed to mimic enclosed environments where additional reactions in the second wall are a significant source of radiation risk, par-

---

*Corresponding author.
Email address:* hratliff@vols.utk.edu (H. N. Ratliff)

ticularly from neutrons.

This paper outlines the experiment and methodologies employed to characterize neutrons produced in the primary, upstream target and details the dependencies of neutron yields on target material, thickness, beam ion and energy. A description of the neutrons produced in the secondary, downstream target, with more emphasis placed on the different methodology used to characterize them, is presented in Reference 3.

2. Experiment and analysis methodologies

A comprehensive description of the experiment with specific information on all dimensions, materials, and equipment can be found in Reference 4. Targets were bombarded with fifteen beams representative of relatively abundant GCR ions and energies. Eight target configurations were used, composed of various mass thicknesses of aluminum and/or high-density polyethylene (HDPE) emulating spacecraft walls, and the secondary particles produced were detected in six cylindrical 5"×5" organic liquid scintillators (OLS) placed at differing angles with respect to the beamline and center of the primary target. Thick target neutron yields were determined for every combination of the following:

- 5 beam species (H, He, C, Si, and Fe)
- 3 energies per species (400, 800, and 1500 MeV/n for Z>1 / 2500 MeV for H)
- 8 primary + secondary target configurations
  - 20 g/cm² Al primary target + 60 g/cm² Al secondary target
  - 40 g/cm² Al primary target + 60 g/cm² Al secondary target
  - 60 g/cm² Al primary target + 60 g/cm² Al secondary target
  - 20 g/cm² HDPE primary target + 60 g/cm² HDPE secondary target
  - 40 g/cm² HDPE primary target + 60 g/cm² HDPE secondary target
  - 60 g/cm² HDPE primary target + 60 g/cm² HDPE secondary target
  - 10 g/cm² Al followed by 10 g/cm² HDPE primary target (referred to as 20 g/cm² AlPE) + 60 g/cm² HDPE secondary target
  - 10 g/cm² Al followed by 50 g/cm² HDPE primary target (referred to as 60 g/cm² AlPE) + 60 g/cm² HDPE secondary target
- 6 detector angles (10°, 30°, 45°, 60°, 80°, and 135°)

A total of 120 combinations of beam projectile and target configurations were used and are summarized in Figure 1, along with a schematic showing the positions of the neutron detectors and targets. The kinetic energies of all particles produced in the upstream target were determined with time-of-flight techniques. Data were acquired on an event-by-event basis and analyzed offline. In each event, the time of flight between a signal in the beam scintillator and the signal in an OLS, the total charge collected in the OLS signal, and charge collected in the first 35 ns of the OLS signal were recorded. The offline analysis was broken into two broad categories: (1) separate good neutron events from all other events and (2) characterize neutron energies from times of flight and quantify uncertainties.

2.1. Detection and off-line analysis of neutrons

Upon entering the experiment room, beam particles first passed through a pair of thin plastic scintillators, referred to as beam scintillators, located upstream of the
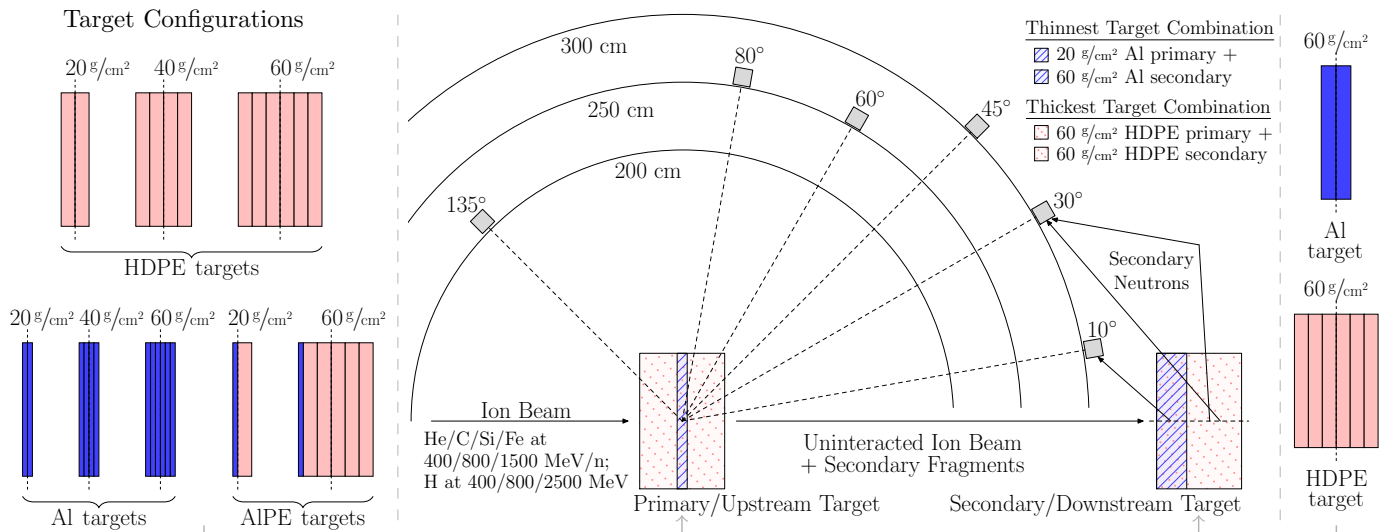

Figure 1: A to-scale schematic of the beam/detector/target system and the 8 primary and 2 secondary target configurations (mass centers indicated with dashed lines); the physically thinnest (hatched blue) and thickest (dotted red) targets are featured in the system drawing.

first target. Requiring signals from these detectors to be consistent with expected signals from primary beam ions allowed for the elimination of events corresponding to incident particles produced in nuclear interactions of beam ions in materials upstream of the target. The number of beam particles incident on the target was also determined using the upstream scintillators; this number is needed for normalization. Upon striking the primary target, the beam either lost energy without undergoing nuclear interactions or produced fragments and other secondary particles if a nuclear interaction occurred. Secondary particles which escaped the target with trajectories bound for one of the six OLS detectors would first pass through a thin (6-mm thick) plastic scintillator placed directly in front of the OLS detectors. An event with a deposited energy signal in the thin scintillator was assumed to be a charged particle event given that the detection efficiency for charged particles in the thin scintillator is 100 percent, whereas the detection efficiency for neutrons is less than 2 percent. As such, an event which had a signal in the OLS but no signal in its accompanying 6-mm plastic scintillator was accepted as either a neutron or gamma ray. Pulse shape discrimination techniques were employed using the OLS signal's total charge and charge in the first 35 ns to separate neutron and photon events [5].

Neutrons detected in the OLS could be attributable to multiple sources: they could come directly from the primary target, from scattering in the room, from the downstream target, or from particle interactions in air and other materials in the room. To separate the primary target-produced neutrons from neutrons attributable to background sources, the experiment employed two iron rods of diameter equal to that of the OLS detectors and of lengths 91 cm and 182 cm, referred to as "shadow bars," to perform background measurements. Deployed in this manner, the shadow bars are highly efficient at absorbing direct neutrons. For a given combination of beam and target, measurements can be made with a shadow bar blocking or not blocking each detector's line-of-sight to the primary target. After normalization, the data taken with the shadow bar present can be subtracted from those without, leaving normalized results for only the neutrons produced in the primary target and directly bound for a detector. Thus, each of the 120 measurement combinations were repeated four times with the two shadow bars placed in the configurations shown in Table 1.

2.2. Implementation of time-of-flight methods and uncertainty analysis

The time of flight for each event was recorded in a time-to-digital convertor (TDC). The absolute time scale in each TDC spectrum was determined using the TDC channel number of the prompt gamma-ray peak that is always present in such spectra. The peaks are created by gamma rays produced by interactions in the target that travel directly to the OLS. Neutron velocity and corresponding kinetic energy were then determined through Equations 1

Table 1: Shadow bar configurations.

Detector angle off beam axis	Setup A	Setup B	Setup C	Setup D
10°	-	x_1	-	-
30°	-	-	x_1	-
45°	-	-	-	x_1
60°	-	x_2	-	-
80°	-	-	x_2	-
135°	-	-	-	x_2

"x" indicates a detector covered by a shadow bar; "-" indicates a detector uncovered. x_1 denotes use of the 182 cm shadow bar while x_2 denotes use of the 91 cm shadow bar.

through 3, where $\Delta t_{n-\gamma}$ is the difference in time between a neutron TDC channel number and the prompt gamma-ray peak channel number.

As shown in Equation 1, t_n is defined as the sum of the photon flight time (d/c, a constant) and the difference of detection times of the two neutral particles in the timing system, $\Delta t_{n-\gamma}$. The flight-path distance d is taken to be the center of the primary target to the center of each OLS detector, and neutrons are assumed to be produced evenly along the length of each target. These are first-order approximations that are refined in subsequent analysis.

$$t_n = \frac{d}{c} + \Delta t_{n-\gamma} \qquad (1)$$

$$v_n = d/t_n \qquad (2)$$

$$E_n = \left(\sqrt{\frac{1}{1 - (v_n/c)^2}} - 1 \right) m_n c^2 \qquad (3)$$

To convert the number of counts in the TDC spectra to double-differential neutron yields, a series of normalizations are applied to the data. Prior to background subtraction, individual measurements are normalized to the data acquisition live time and the number of beam particles which were of the prescribed species and energy. Then, all measurements for each combination of beam, target configuration, and detector are combined, with non-shadow bar measurements combined separately from shadow measurements for each detector. The normalized, combined shadow bar measurement is then subtracted from the normalized non-shadow bar measurement. The spectra are then corrected for the energy-dependent intrinsic neutron detection efficiency of the OLS detectors using efficiency curves generated with the SCINFUL-QMD code [6]. Afterward, the channels are normalized to solid angle and then rebinned to fulfill a number of criteria based on desired statistical uncertainty, number of energy bins, energy bin spacing, intrinsic timing resolution and minimized energy resolution uncertainties. Finally, the spectra are normalized to energy bin width, resulting in the final double-differential yield values.

These results are subject to both statistical and systematic uncertainties. The statistical uncertainty in each final yield value is calculated using Poisson statistics (converged to Gaussian distributions for bins with sufficiently high counts). Three components of systematic uncertainty were isolated in this work. First, a flat 10% uncertainty is assumed in the efficiency correction performed using SCINFUL-QMD-generated efficiency curves [6, 7, 8]. Second, each final value possesses a systematic uncertainty attributable to the human judgment involved in the data analysis process, such as the delineation of gamma-ray events from neutron events in two-dimensional pulse shape plots; this is calculated by first repeating the steps requiring human input and all subsequent analysis and then taking the fractional difference between the initial and this second calculation of each value. This uncertainty component is typically a few percent or lower. Third, a systematic uncertainty is present in the solid angle normalization since neutrons from the primary target can be produced anywhere along its length; this is sometimes the dominant component of systematic uncertainty due to the fairly large thicknesses of the targets relative to the total flight-path length and typically ranges from 5% to 15% (but can be as high as 23%) depending on the detector position and target thickness.

In addition to uncertainties in the yield axis, there is also uncertainty in the neutron energy axis. This is expressed as energy resolution uncertainty $\Delta E_n/E_n$ and is a function of the neutron kinetic energy E_n, flight path uncertainty $\Delta L/L$ (stemming from the range of possible neutron production points along the length of the primary target), intrinsic timing resolution $\Delta t/t$, neutron velocity β ($\beta = v_n/c$), and neutron mass m_n as shown in Equation 4 [8].

$$\frac{\Delta E_n}{E_n} = \frac{E_n + m_n c^2}{E_n} \frac{\beta^2}{1 - \beta^2} \sqrt{\left(\frac{\Delta L}{L}\right)^2 + \left(\frac{\Delta t}{t}\right)^2} \quad (4)$$

Treating the average neutron flight distance d as a constant is, in some cases, a poor approximation. This stems from the initial assumption that all neutrons were produced, on average, at the center of the primary target. In reality, the neutron production distribution within the targets is a function of beam species, beam energy, target material(s), target thickness, and secondary neutron energy. To correct for this, every projectile and target combination was simulated in the PHITS particle transport code [9], and the distribution of neutrons produced within each primary target was tallied as a function of depth in target and neutron energy. These simulated results were used to find the median depth of neutron production as a function of neutron energy for every measured projectile and target combination. These new values were taken to be the production points used in the final time-of-flight, solid angle, and energy resolution uncertainty calculations. This correction has the largest impact on the highest energy neutrons (especially those above the beam energy) and on the least penetrating beams, for which neutron production tends to be concentrated toward the upstream face of the primary target. Shifting the assumed production point upstream results in increased flight paths to the downstream detectors and thus increased neutron energies compared to the original calculation.

Similarly, the simulated neutron production distributions can be used to refine the assumption that neutrons are produced evenly throughout the whole length of each target. While neutron production along the length of a target is usually somewhat evenly distributed for lower and intermediate energy neutrons and for the more penetrating beams, this ceases to be the case for less penetrating beams and, most importantly, the highest energy neutrons. As seen earlier in Equation 4, the energy resolution uncertainty becomes increasingly sensitive to both the intrinsic timing resolution (which is a constant) and the flight path uncertainty as neutron energy increases. Thus, making a less conservative and more realistic assumption on what region of the target contains a majority of the neutrons produced can greatly reduce this uncertainty at higher energies. Thus, the final calculations used the smallest length of each target containing 80% of all neutrons produced at each energy as the "effective target thickness," improving both the energy resolution and solid angle uncertainties, particularly for the highest energy neutrons. This methodology of generating and implementing updated production point and effective target thickness assumptions is covered in greater detail in Reference 10. More discussion on the analysis procedures can be found in References 10 and 11.

3. Results

At the beam energies in these experiments, fragmentation is the most prominent reaction mechanism occurring upon the collision of projectile and target nuclei. These reactions are described in this work with the abrasion-ablation model [12, 13]. Prior to the collision, the two-body system is treated as a projectile in motion approaching a target at rest. Upon colliding with some degree of overlap (ranging from peripheral to central) of the two nuclei, three fragments are produced in the abrasion (cascade) stage: a target fragment (still relatively at rest), a projectile fragment (still traveling at or near its initial velocity), and a "fireball" or intermediate rapidity source composed of nucleons in the overlap region of the two nuclei (as seen from behind the projectile nucleus along its momentum vector). This is immediately followed by the ablation (evaporation) stage wherein the three excited nucleon agglomerates de-excite by ejecting (or "boiling off") nucleons. In very peripheral reactions, only a few nucleons can be sheared off, but more direct collisions can result in a complete dissociation of both nuclei involved.

The fireball has momentum in the same direction as the projectile but with a magnitude of about one third to half

that of the projectile [14]. Additionally, while the evaporation process is fairly isotropic in the reference frame of each fragment [15], the momentum of each ejected nucleon in the lab frame is largely dominated by that of its source fragment.

Due to the large volume of data present for the upstream target-produced neutrons (720 spectra in total), a representative look at the impact of each experimental variable (beam ion species, beam ion energy, target thickness and material) on neutron yield is presented here as opposed to a comprehensive listing of all spectra. While exceptions do exist for the trends described here due to the complexity of the multiple layers of physics present, the plots and trends presented are representative of the majority. The individual points on each plot in this section contain the information detailed in Figure 2, where each point is encompassed in a shaded box whose height denotes statistical uncertainty (1σ) and width denotes the energy resolution uncertainty and is overlaid with a cross whose vertical bar denotes systematic uncertainty and horizontal bar denotes the energy bin width.
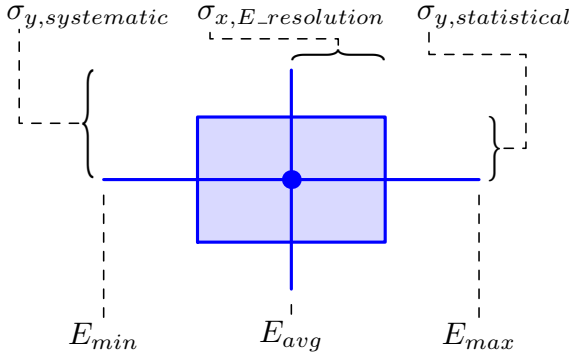
Figure 2: Explanation of each plotted energy bin [10].

The experimental variable studied first is the effect of projectile species, depicted in Figure 3 for all projectiles at 400 MeV/n incident upon the 20 g/cm^2 AlPE hybrid target for neutrons seen in the 10° detector. In these figures, "s.p." stands for "source particle."
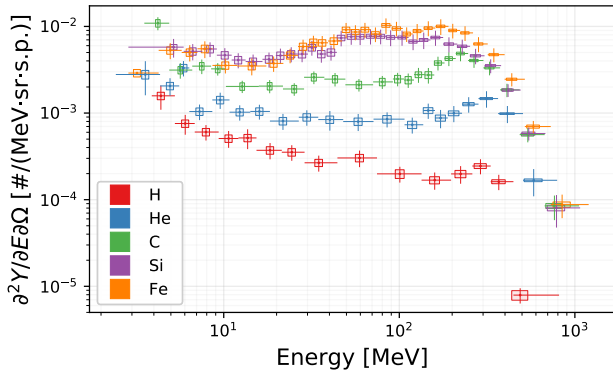

Figure 3: Neutrons detected at 10° from all 400 MeV/n projectile species incident on the 20 g/cm^2 AlPE upstream target.

For projectiles of the same kinetic energy per nucleon

but of varying mass, neutron yields scale with projectile mass. The difference in yields is, at most, a two-order of magnitude difference between iron and hydrogen projectiles. The difference in the yield due to projectile mass is most severe with the thinnest targets and becomes less extreme with the thicker targets where the heavier projectiles and their secondary particles have comparatively short ranges in the primary target, as shown in Figure 4 for the same projectiles incident upon the 60 g/cm^2 AlPE hybrid target. This trend is true for all target materials tested.
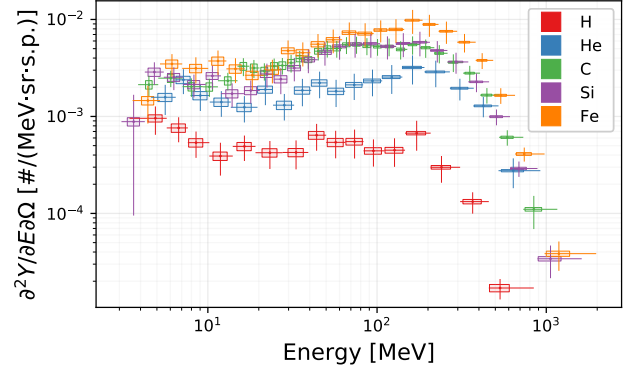

Figure 4: Neutrons detected at 10° from all 400 MeV/n projectile species incident on the 60 g/cm^2 AlPE upstream target.

Figures 3 and 4 show spectra seen at the 10° detector, the smallest angle measured, where the spectrum is dominated by projectile fragments. The high energy neutrons are from projectile fragmentation, and, due to the Fermi motion of the nucleons within the projectile nucleus, individual nucleons can attain velocities in the lab frame that exceed that of the beam ions. Thus, when neutrons are sheared off or evaporated from the projectile fragment, retaining their prior momentum, some leave the interaction with more kinetic energy than the beam energy (per nucleon). This effect is increasingly significant as projectile mass increases and can be seen in these figures by noting the maximum observed neutron energies.

The impact of the projectile fragment, characteristic of the high-energy portion of the spectra, diminishes sharply with increasing detector angle, as seen in Figure 5 for neutrons detected at all angles from 400 MeV/n Si incident on the 20 g/cm^2 HDPE primary target. Since the target fragment remains relatively at rest, isotropic evaporation products are seen at all angles at lower energies, and dominate these portions of the spectra. While the yield spectra do mostly converge at lower energies, as expected for isotropic target evaporation, it appears that the 60°, 135°, and especially 80° spectra are depressed in comparison to the smaller angles. Given the shape and physical width of the targets, this relative depression is attributable to the greater amount of target material that secondary neutrons must pass through to reach these detectors, causing some attenuation of the expected yield.

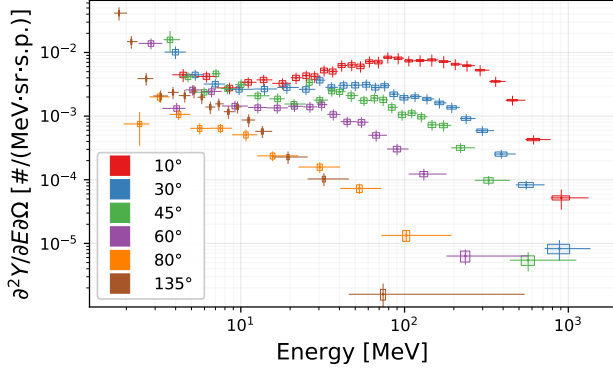When studying the impact of projectile energy on neu-

Figure 5: Neutrons detected at all angles from 400 MeV/n Si projectiles incident on the 20 g/cm² HDPE upstream target.

tron yields, some experimental challenges and limitations are present. Figure 6 shows the three spectra for neutrons in the 10° detector from the three energies of Si incident upon the 20 g/cm² HDPE primary target. Due to the available beam currents at NSRL being highest for the lower energy beams, statistical uncertainties were typically better for the 400 MeV/n projectiles than for the others, as evidenced by the density of points for each energy in Figure 6.

Additionally, higher beam energies resulted in greater neutron background from additional reactions in the secondary target. In the case of the 10° detector, located close to the secondary target, this increased background in some cases adversely affected the performance of the background subtraction; this is the cause of the fairly large fluctuations and missing point around 200 MeV in the 1500 MeV/n projectile spectrum of Figure 6. An upper limit in neutron energy around 1 GeV was due to the limited flight paths possible in the experiment room at NSRL and the ability to properly distinguish prompt photons from highly relativistic neutrons. These two limitations were present almost exclusively for the data from the 10° detector; and the issue of overwhelming background is only present in the 1500 MeV/n Si and Fe projectile cases.
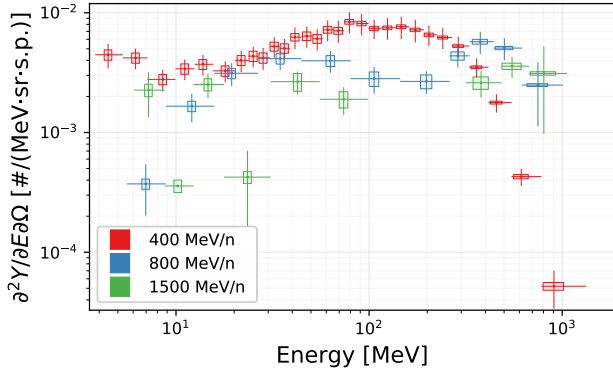

Figure 6: Neutrons detected at 10° from all Si projectile energies incident on the 20 g/cm² HDPE upstream target.

The impact of projectile energy is best observed in the

data from the carbon projectiles. The yields from the thinnest and thickest aluminum upstream targets for all three carbon energies are shown in Figures 7a and 7b. While, intuitively, the highest neutron yields should be generated from the highest energy beams since they can penetrate the target, resulting in a greater number of reactions, this is not evident here due to the range of neutron energies that can be detected, causing a premature cutoff in the 800 MeV/n and 1500 MeV/n projectile cases. However, when comparing Figure 7b with Figure 7a, the thicker target allows for a more notable buildup of lower energy target fragmentation neutrons as beam energy increases.
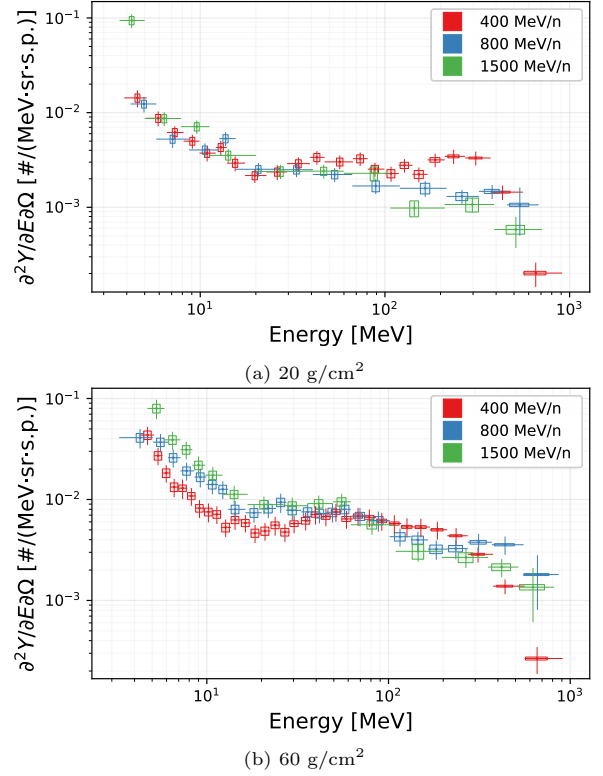

(a) 20 g/cm²

(b) 60 g/cm²

Figure 7: Neutrons detected at 10° from C projectiles incident on the 20 g/cm² and 60 g/cm² Al upstream targets.

Comparison of the two different target materials of the same areal density showed high-density polyethylene resulted in consistently lower yields than aluminum targets; this is highlighted in Figure 8 for 400 MeV/n ¹²C beams incident upon the minimum and maximum thicknesses of each of the three material configurations. Pure aluminum targets resulted in comparatively large neutron yields at the lowest energies due to more significant target fragment evaporation. One interesting observation is the performance of the hybrid AlPE targets—intended to mimic a more "realistic" spacecraft composed of an aluminum shell with plastics and other hydrogenous materials inside the shell—relative to pure aluminum or HDPE. The hybrid target material generally produced similar or even lower neutron yields than pure HDPE. While one would expect

the 60 g/cm² AlPE target to behave more like HDPE than aluminum due to being 10 g/cm² Al followed by 50 g/cm² HDPE, it is notable that even for the 20 g/cm² AlPE target, which is composed of half of each material, the neutron yields still more closely resemble those of the pure HDPE targets in most cases.
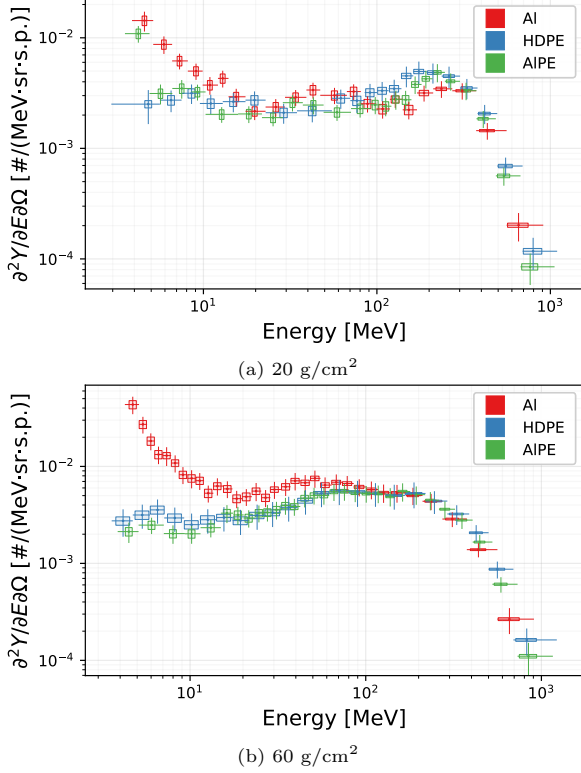

(a) 20 g/cm²

(b) 60 g/cm²

Figure 8: Neutrons detected at 10° from 400 MeV/n C projectiles incident on the three materials of each upstream target for the 20 g/cm² and 60 g/cm² thicknesses.

Similar thick-target experiments in the past have generally focused on using single stopping targets [16, 17] relevant to shielding for terrestrial application, but the use of dual target system with a variable primary target thickness is particularly relevant to spacecraft where the primary GCR is isotropic and incident ions will traverse different paths and different thicknesses when entering the spacecraft. The dependence of neutron yields on target thickness is related to the penetrability of the incident beams, and if it stops, how deep into the target a beam goes before stopping. In general, it is expected that the highest neutron yields are produced when the number of interactions in a target is maximized, meaning thicker targets would result in the highest yield. This is the case for beams which do fully penetrate the upstream target but is not necessarily true for beams which stop in the primary target. Shown in Figure 9 for 400 MeV/n C incident upon the three thicknesses of pure Al and HDPE targets, where it can be seen that yield is lowest from the 20 g/cm² targets but very similar for the 40 g/cm² and 60 g/cm² thicknesses. This is because the beam penetrates the 20 g/cm²

thickness but is stopped by the two thicker targets (range of 35.8 g/cm² in Al and 26.5 g/cm² in HDPE), maximizing the number of interactions.
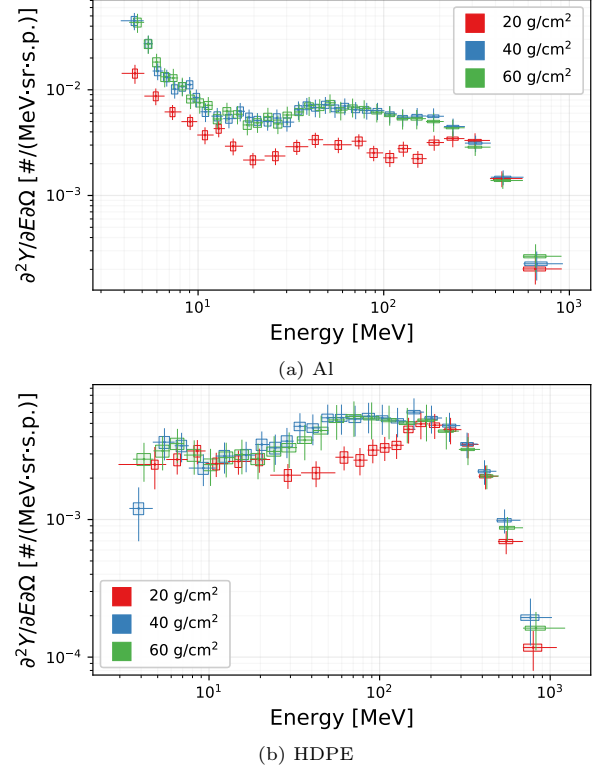

(a) Al

(b) HDPE

Figure 9: Neutrons detected at 10° from 400 MeV/n C projectiles incident on the three thicknesses of each pure upstream target.

To highlight a case where primary target neutron yield scales with target thickness, Figure 10 shows the results obtained with the 800 MeV/n Si beam incident on the Al and HDPE targets. Here, the beam ions only penetrate the 20 g/cm² Al, 40 g/cm² Al, and 20 g/cm² HDPE primary targets before stopping. Unlike the previous example, though, 60 g/cm² HDPE still results in higher neutron yields than 40 g/cm² HDPE despite the beam ions stopping in both targets. This effect is due to fragmentation of the primary beam creating lighter mass secondary particles which can penetrate deeper into the target, creating additional neutrons via secondary interactions. If the lighter mass secondary particles penetrate the primary target, they then can produce additional neutrons via interactions in the secondary, downstream target and in the air between the two targets.

The reverse of this trend is shown in Figure 11 where the 400 MeV/n Si beam is stopped in all targets. The velocity and species of the projectile fragments (and the nucleons ejected) are still determined by the initial beam. In this case, most of the secondary and tertiary fragments do not penetrate the remainder of target material in their paths, maximizing the number of neutrons produced in the targets. Thus, the primary factor differentiating neutron yields for varying target thicknesses is the neutron moder-
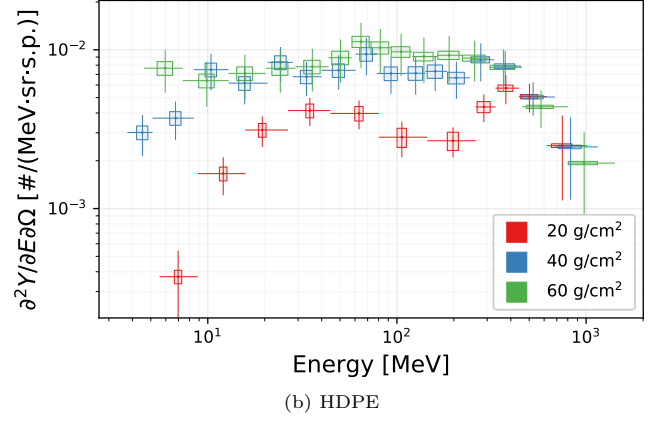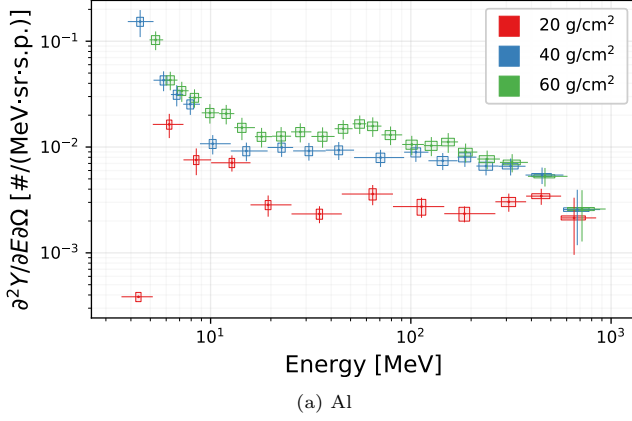
Figure 10: Neutrons detected at 10° from 800 MeV/n Si projectiles incident on the three thicknesses of each pure upstream target.
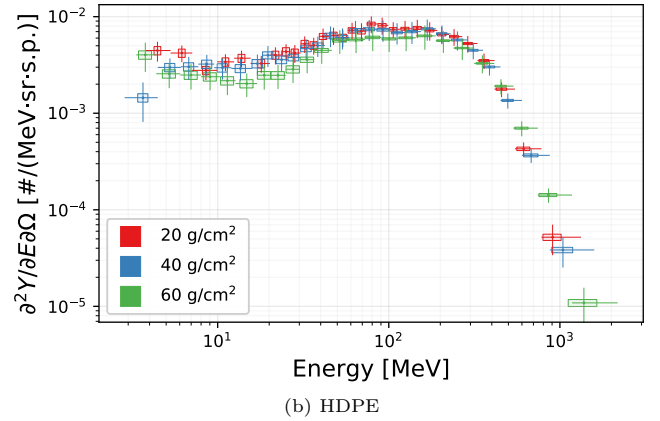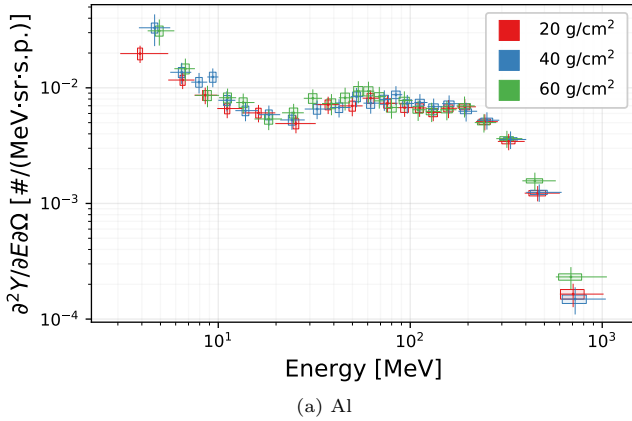

Figure 11: Neutrons detected at 10° from 400 MeV/n Si projectiles incident on the three thicknesses of each pure upstream target.

ating capability of the target materials. As seen in Figure 11b, the increasing thickness of HDPE, a material known for its moderation properties, has a notable impact on neutron yield; this is not the case in Figure 11a for aluminum which is largely transparent to neutrons in comparison.

4. Conclusions

The systematics of neutron production from GCR-like beams incident on several thick targets composed of Al and HDPE were studied as part of a larger experimental effort to develop a benchmark dataset for GCR-like intermediate-energy heavy ions incident upon spacecraft-like thick targets; specifically featured in this work was the portion of this dataset encompassing neutrons produced in the primary upstream target in a two-target system. This data along with other data generated from the experiment are useful for comparisons to transport model calculations to evaluate the uncertainties associated with those calculations and to provide guidance for possible improvements to those codes. Evaluating the performance of some Monte Carlo transport codes in reproducing the results of this benchmark dataset will be the subject of future work.

The time-of-flight techniques employed for determining the neutron spectra from the primary target are stan-dard methods used in neutron time-of-flight experiments. Issues arising from the targets of significant thickness relative to the total neutron flight paths required the development of novel techniques to improve upon assumptions made about the interaction point in the target, with consequent reduction in the systematic uncertainties in the results. This involved the development of continuous neutron energy-dependent production point and effective target thickness calculations utilizing PHITS simulations of the neutron production distributions within each target for every combination of beam and target that was experimentally tested. Additional efforts were also made to decouple target thickness from timing resolution in the calculation of energy resolution.

Discussion of the neutrons produced in the secondary downstream target, a unique facet of this experiment, is contained in a following paper, Reference 3. The entire primary target neutron dataset, along with the secondary target neutrons data sets, are available through several outlets online.

The repository containing all of the experimental results will be made available from the University of Tennessee's TRACE repository and is also available per request to the author. Additionally, an online tool developed by the author, called SHAEDIT [18], is available at

CRediT authorship contribution statement

Hunter N. Ratliff: Conceptualization, Methodology, Software, Formal analysis, Investigation, Data Curation, Writing - Original Draft, Visualization. **Natalie A. Mc-Girl:** Conceptualization, Methodology, Software, Formal analysis, Investigation. **Matthew R. Beach:** Software, Investigation, Data Curation. **Luis A. Castellanos:** Software, Investigation, Data Curation. **Martha S. Clowdsley:** Investigation, Supervision, Project administration, Funding acquisition. **Lawrence H. Heilbronn:** Conceptualization, Investigation, Resources, Writing - Review & Editing, Supervision, Project administration, Funding acquisition. **Chiara LaTessa:** Conceptualization, Investigation. **John W. Norbury:** Conceptualization, Supervision. **Adam Rusek:** Conceptualization, Investigation, Resources. **Michael Sivertz:** Conceptualization, Investigation, Resources. **Ashwin P. Srikrishna:** Investigation. **Hui-Chen Wang:** Investigation. **Cary Zeitlin:** Conceptualization, Investigation, Writing - Review & Editing, Supervision, Project administration, Funding acquisition.

Acknowledgments

References

[1] T. C. Slaba, A. A. Bahadori, B. D. Reddell, R. C. Singleterry, M. S. Clowdsley, S. R. Blattnig, Optimal shielding thickness for galactic cosmic ray environments, Life Sciences in Space Research 12 (2017) 1–15. doi:10.1016/j.lssr.2016.12.003.

[2] ICRP, ICRP publication 60: 1990 recommendations of the International Commission on Radiological Protection, no. 60, Elsevier Health Sciences, 1991.

[3] H. N. Ratliff, N. A. McGirl, M. R. Beach, L. A. Castellanos, M. S. Clowdsley, L. H. Heilbronn, C. LaTessa, J. W. Norbury, A. Rusek, M. Sivertz, A. P. Srikrishna, H.-C. Wang, C. Zeitlin, Development of scalable deconvolution methods for determining secondary target neutron yields from dual-thick-target cosmic-ray ion accelerator experiments, Nucl. Instrum. Methods Phys. Res., B, *submitted concurrently*.

[4] L. H. Heilbronn, C. Zeitlin, M. R. Beach, L. A. Castellanos, M. S. Clowdsley, C. LaTessa, N. A. McGirl, J. W. Norbury, H. N. Ratliff, A. Rusek, M. Sivertz, A. P. Srikrishna, H.-C. Wang, Design of an accelerator-based experiment relevant to enclosed, shielded environments in space, Nucl. Instrum. Methods Phys. Res., B, *submitted concurrently*.

[5] J. H. Heltsley, L. Brandon, A. Galonsky, L. Heilbronn, B. A. Remington, S. Langer, A. V. Molen, J. Yurkon, J. Kasagi, Particle identification via pulse-shape discrimination with a charge-integrating ADC, Nucl. Instrum. Methods Phys. Res., A 263 (2) (1988) 441–445. doi:10.1016/0168-9002(88)90984-9.

[6] D. Satoh, S. Kunieda, Y. Iwamoto, N. Shigyo, K. Ishibashi, Development of SCINFUL-QMD code to calculate the neutron detection efficiencies for liquid organic scintillator up to 3 GeV, Journal of Nuclear Science and Technology 39 (sup2) (2002) 657–660. doi:10.1080/00223131.2002.10875185.

[7] P.-E. Tsai, Study of secondary particles produced from heavy-ion interactions, Ph.D. thesis, The University of Tennessee, Knoxville (2015).

[8] T. Nakamura, L. Heilbronn, Handbook on Secondary Particle Production and Transport by High-energy Heavy Ions:(with CD-ROM), World Scientific, 2006. doi:10.1142/5973.

[9] T. Sato, Y. Iwamoto, S. Hashimoto, T. Ogawa, T. Furuta, S. ichiro Abe, T. Kai, P.-E. Tsai, N. Matsuda, H. Iwase, N. Shigyo, L. Sihver, K. Niita, Features of Particle and Heavy Ion Transport code System (PHITS) version 3.02, Journal of Nuclear Science and Technology 55 (6) (2018) 684–690. doi:10.1080/00223131.2017.1419890.

[10] H. N. Ratliff, Thick-target neutron yields for intermediate-energy heavy ion experiments at NSRL, Ph.D. thesis, The University of Tennessee, Knoxville (2018).

[11] N. A. McGirl, Double differential neutron yields produced by proton, helium, and iron interactions in thick aluminum targets, Ph.D. thesis, The University of Tennessee, Knoxville (2017).

[12] L. W. Townsend, J. W. Wilson, J. W. Norbury, H. B. Bidasaria, An abrasion-ablation model description of galactic heavy-ion fragmentation, NASA technical paper, National Aeronautics and Space Administration, Scientific and Technical Information Branch, 1984.
URL https://ntrs.nasa.gov/citations/19840014328

[13] F. A. Cucinotta, J. W. Wilson, L. W. Townsend, Abrasion-ablation model for neutron production in heavy ion collisions, Nuclear Physics A 619 (1) (1997) 202–212. doi:10.1016/S0375-9474(97)00130-9.

[14] Y. Iwata, T. Murakami, H. Sato, H. Iwase, T. Nakamura, T. Kurosawa, L. Heilbronn, R. M. Ronningen, K. Ieki, Y. Tozawa, K. Niita, Double-differential cross sections for the neutron production from heavy-ion reactions at energies $E/A = 290 - 600$ MeV, Phys. Rev. C 64 (2001) 054609. doi:10.1103/PhysRevC.64.054609.

[15] J. Gosset, H. H. Gutbrod, W. G. Meyer, A. M. Poskanzer, A. Sandoval, R. Stock, G. D. Westfall, Central collisions of relativistic heavy ions, Phys. Rev. C 16 (1977) 629–657. doi:10.1103/PhysRevC.16.629.

[16] T. Kurosawa, N. Nakao, T. Nakamura, H. Iwase, H. Sato, Y. Uwamino, A. Fukumura, Neutron yields from thick C, Al, Cu, and Pb targets bombarded by 400 MeV/nucleon Ar, Fe, Xe and 800 MeV/nucleon Si ions, Phys. Rev. C 62 (2000) 044615. doi:10.1103/PhysRevC.62.044615.

[17] L. Heilbronn, T. Nakamura, Y. Iwata, T. Kurosawa, H. Iwase, L. W. Townsend, Overview of secondary neutron production relevant to shielding in space, Radiation Protection Dosimetry 116 (1-4) (2005) 140–143. doi:10.1093/rpd/nci033.

[18] H. N. Ratliff, SHAEDIT: Space Hadron Accelerator Experiment Data Investigation Tool (2018). doi:10.5281/zenodo.1291203.
URL https://github.com/Lindt8/SHAEDIT